(1) The correlation of kinetic and entropy-based thermodynamic fragilities is implied by the repeated analyses of the calorimetric and kinetic behaviour of liquids (not polymers) of different classes that extract 'ground state temperatures' from the data and find them to have very similar values. We refer to T_K (where the supercooling liquid entropy extrapolates to the crystal entropy) and T_o (where the viscosity extrapolates to infinity by the Vogel–Fulcher–Tammann equation). Ref. 17 describes some 30 cases where $T_o = T_K$ within ± 3% despite several pronounced exceptions). As the ratio T_g / T_o is often taken as a measure of fragility[17], it is clear that $T_K \approx T_o$ implies that kinetic fragility and thermodynamic fragility T_g/T_K are the same, with some pronounced exceptions. This means that either the physically constrained analysis leading to $T_o \approx T_K$ is flawed, or that the analysis of Ngai[3] and co-workers, being limited to dielectric relaxation of molecular liquids, and containing some misplots (see Fig. 3 legend), has distorted the overall picture.

(2) $T_o \approx T_K$ is also a recent result of MD computer-simulation studies on well defined systems[11–13]. Although the number of systems studied is small, the results are important because the identity of T_o and T_K is obtained using all-amorphous phase calculations; that is, there is no reliance on fusion entropy data.

(3) Both of the above arguments are weakened by the fact that they depend on extrapolations beyond the range of experimental or simulation data. To avoid this, and at the same time to obtain a more complete picture than given in refs 2 and 3, we compare wide-ranging data on some 25 liquids from the fields of geochemistry (liquid silicates), covalent semiconductors (liquid chalcogenides), molecular liquids, and molten ionic hydrates, salts and oxides, and including all the systems analysed by Ngai and Yamamuro[3]. Unlike the cases in ref. 3, the present data set covers the whole known fragility range. The quantities studied are the shear viscosities and the excess of the liquid entropy over the crystal entropy measured at the same temperature, and uncorrected in any manner. We note that S_{ex} in ref. 22 is not the same quantity as in the present work. It requires quantitative knowledge of the residual entropy at 0 K for its assessment. Also, in ref. 26 an attempt was made to separate out vibrational contributions to the entropy of the liquid above T_g in order to obtain S_c (for use in the Adam–Gibbs equation (equation (1)) by using a function fitted to the heat capacity of the glass. This yields a quantity which is neither S_c nor S_{ex} because the procedure does not consider the introduction of new low frequencies above T_g, which is central to our conclusions.

The quality of data used in this study is variable, ranging from very high, in the case of adiabatic calorimetry data on molecular liquids (data cited in ref. 3) and some high temperature substances (B_2O_3), to moderate, in the case of high-temperature differential scanning calorimeter (DSC) and drop calorimetry data on minerals. Reference sources are available from the authors. Both data sets are presented (Figs 1 and 2) as functions of inverse temperature scaled by the calorimetric onset T_g for the substance, as measured during upscan at 10 K min^{-1} (after previous continuous cooling at the same rate). This corresponds to scaling by the temperature at which the enthalpy relaxation time is approximately 200 s (refs 17, 18).

Received 10 November 2000; accepted 29 January 2001.

1. Angell, C. A. Relaxation in liquids, polymers and plastic crystals - strong/fragile patterns and problems. *J. Non-Cryst. Solids* **131-133,** 13–31 (1991).
2. Ito, K., Moynihan, C. T. & Angell, C. A. Thermodynamic determination of fragility in liquids and a fragile-to-strong liquid transition in water. *Nature* **398,** 492–495 (1999).
3. Ngai, K. L. & Yamamuro, O. Thermodynamic fragility and kinetic fragility in supercooled liquids: a missing link. *J. Chem. Phys.* **111,** 10403–10406 (1999).
4. Sastry, S., Debenedetti, P. G. & Stillinger, F. H. Signatures of distinct dynamical regimes in the energy landscape of a glassforming liquid. *Nature* **393,** 554–557 (1998).
5. Speedy, R. J. Relations between a liquid and its glasses. *J. Phys. Chem. B* **103,** 4060–4065 (1999).
6. Roland, C. M., Santangelo, P. G. & Ngai, K. L. The application of the energy landscape model to polymers. *J. Chem. Phys.* **111,** 5593–5598 (1999).
7. Speedy, R. J. The hard sphere glass transition. *Mol. Phys.* **95,** 169–178 (1998).
8. Sciortino, F., Kob, W. & Tartaglia, P. Inherent structure entropy of supercooled liquids. *Phys. Rev. Lett.* **83,** 3214–3217 (1999).
9. Buechner, S. & Heuer, A. The potential energy landscape of a model glassformer: thermodynamics, anharmonicities, and finite size effects. *Phys. Rev. E* **60,** 6507–6518 (1999).
10. Coluzzi, B., Verrocchio, P., Mezard, M. & Parisi, G. Lennard-Jones binary mixture: a thermodynamical approach to glass transition. *J. Chem. Phys.* **112,** 2933–2944 (2000).
11. Scala, A., Starr, F., La Nave, E., Sciortino, F. & Stanley, H. E. Configurational entropy and diffusion of supercooled water. *Nature* **406,** 166–169 (2000).
12. Sastry, S. Liquid limits: the glass transition and liquid-gas spinodal boundaries of metastable liquids. *Phys. Rev. Lett.* **85,** 590–593 (2000).
13. Sastry, S. The relationship between fragility, configurational entropy and the potential energy landscape of glassforming liquids. *Nature* **409,** 164–167 (2001).
14. Richet, P. Viscosity and configurational entropy of silicate melts. *Geochim. Cosmochim. Acta* **48,** 471–483 (1984).
15. Richet, P. & Bottinga, Y. Glass transitions and thermodynamic properties of amorphous SiO_2, $NaAlSi_nO_{2n+2}$ and $KAlSi_3O_8$. *Geochim. Cosmochim. Acta* **48,** 453–470 (1984).
16. Adam, G. & Gibbs, J. H. On the temperature dependence of cooperative relaxation properties in glassforming liquids. *J. Chem. Phys.* **43,** 139–146 (1965).
17. Angell, C. A. Entropy and fragility in supercooled liquids. *J. Res. NIST* **102,** 171–185 (1997).
18. Richert, R. & Angell, C. A. Dynamics of glassforming liquids. IV: On the link between molecular dynamics and configurational entropy. *J. Chem. Phys.* **108,** 9016–9026 (1998).
19. Goldstein, M. Viscous liquids and the glass transition: a potential energy barrier picture. *J. Chem. Phys.* **51,** 3728–3729 (1969).
20. Stillinger, F. H. & Weber, T. A. Packing structures and transitions in liquids and solids. *Science* **225,** 983–989 (1984).
21. Goldstein, M. Viscous liquids and the glass transition: sources of the excess heat capacity. *J. Chem. Phys.* **64,** 4767–4773 (1976).
22. Johari, G. P. Contributions to the entropy of a glass and liquid, and the dielectric relaxation time. *J. Chem. Phys.* **112,** 7518–7523 (2000).
23. Greet, R. J. & Turnbull, D. Test of Adam-Gibbs liquid viscosity model with *o*-terphenyl specific-heat data. *J. Chem. Phys.* **47,** 2185–2190 (1967).
24. Magill, J. H. Physical properties of aromatic hydrocarbons. III. A test of the Adam-Gibbs relaxation model for glass formers based on the heat-capacity data of 1,3,5-tri-α-naphthylbenzene. *J. Chem. Phys.* **47,** 2802–2807 (1967).
25. Takahara, S., Yamamuro, O. & Suga, H. Heat capacities and glass transitions of 1-propanol and 3-methyl pentane: new evidence for the entropy theory. *J. Non-Cryst. Solids* **171,** 259–270 (1994).
26. Takahara, S., Yamamuro, O. & Matsuo, T. Calorimetric study of 3-bromopentane—correlation between structural relaxation time and configurational entropy. *J. Phys. Chem.* **99,** 9580–9592 (1995).
27. Angell, C. A. Liquid landscapes. *Nature* **393,** 521–522 (1998).
28. Starr, F. W. *et al.* Thermodynamic and structural aspects of the potential energy surface of simulated water. *Phys. Rev. E.* (in the press); also preprint arXiv:cond-mat/0007487 on ⟨xxx.lanl.gov⟩ (2000).
29. Phillips, W. A., Buchenau, U., Nücker, N., Dianou, A. J. & Petry, W. Dynamics of glassy and liquid selenium. *Phys. Rev. Lett.* **63,** 2381–2384 (1989).
30. Wischnewski, A., Buchenau, U., Dianoux, A. J., Kamitakahara, W. A. & Zarestky, J. L. Neutron scattering analysis of low-frequency modes in silica. *Phil. Mag. B* **77,** 579–589 (1998).
31. Kob, W., Sciortino, F. & Tartaglia, P. Aging as dynamics in configuration space. *Europhys. Lett.* **49,** 590–596 (2000).

Acknowledgements

We thank S. Sastry, R. Speedy and F. Sciortino for comments and criticisms. This work was supported by the NSF, Division of Materials Research, Solid State Chemistry program.

Correspondence and requests for materials should be addressed to C.A.A. (e-mail: caa@asu.edu).

Intermittent dislocation flow in viscoplastic deformation

M.-Carmen Miguel*†, Alessandro Vespignani*, Stefano Zapperi‡, Jérôme Weiss§ & Jean-Robert Grasso‖

** The Abdus Salam International Centre for Theoretical Physics, PO Box 586, 34100 Trieste, Italy*
† Departament de Física Fonamental, Facultat de Física, Universitat de Barcelona, Av. Diagonal 647, 08028 Barcelona, Spain
‡ INFM, Università "La Sapienza", P. le A. Moro 2, 00185 Roma, Italy
§ LGGE-CNRS, 54 rue Moliére, BP 96, 38402 St Martin d'Héres Cedex, France
‖ LGIT, BP 53X, 38041 Grenoble Cedex 9, France

The viscoplastic deformation (creep) of crystalline materials under constant stress involves the motion of a large number of interacting dislocations[1]. Analytical methods and sophisticated 'dislocation dynamics' simulations have proved very effective in the study of dislocation patterning, and have led to macroscopic constitutive laws of plastic deformation[2–9]. Yet, a statistical analysis of the dynamics of an assembly of interacting dislocations has not hitherto been performed. Here we report acoustic emission measurements on stressed ice single crystals, the results of which indicate that dislocations move in a scale-free intermittent fashion. This result is confirmed by numerical simulations of a model of interacting dislocations that successfully reproduces the main features of the experiment. We find that dislocations generate a slowly evolving configuration landscape which coexists with rapid collective rearrangements. These rearrangements involve a comparatively small fraction of the dislocations and lead to an intermittent behaviour of the net plastic response. This basic dynamical picture appears to be a generic feature in the deformation of many other materials[10–12]. Moreover, it should provide a framework for discussing fundamental aspects of plasticity that goes beyond standard mean-field approaches that see plastic deformation as a smooth laminar flow.

Whenever dislocation glide is the dominant plastic deformation mechanism in a crystalline material, we observe a constant strain-rate regime usually described by Orowan's relation $\dot{\gamma} \approx \rho_m b v$. Here, the plastic strain-rate of the material $\dot{\gamma}$ is simply related to average quantities such as ρ_m, the density of mobile dislocations, and v, their

average velocity along the slip direction (parallel to the Burgers vector b)[1]. Transmission electron micrographs of plastically deformed materials display, on the other hand, complex features such as cellular structures and fractal patterns[2,3], which are the fingerprint of a complex multiscale dynamics not appropriately accounted for by the mean-field character of Orowan's relation. In addition, rapid slip events[10] have been observed in the plastic deformation of various metals and alloys[11,12], and in the Portevin–LeChatelier effect[13]. We believe that formulating plastic deformation as a nonequilibrium statistical mechanics problem[14] requires a substantial understanding of basic collective dislocation dynamics.

Experimentally, the complex character of collective dislocation dynamics can be revealed by acoustic emission measurements. The acoustic waves recorded in a piezoelectric transducer disclose the pulse-like changes of the local displacements in the material during plastic deformation, whereas a smooth plastic flow would not be detected[15]. Thus, this method is particularly useful for inspecting possible fluctuations in the dislocation velocities and densities.

Ice single crystals can be used as a model material to study glide dislocation dynamics by acoustic emission (refs 16, 17) for the following reasons: (1) Transparency allows direct verification that acoustic emission activity is not related to microcracking. (2) Within the range of temperature and stress corresponding to our experimental conditions, diffusional creep is not a significant mechanism of inelastic deformation[18] which, in hexagonal ice single crystals, occurs essentially by dislocation glide on the basal planes along a preferred slip direction. (3) An excellent coupling between sample and transducer can be obtained by fusion/freezing.

Uniaxial compression creep experiments are performed on artificial ice single crystals, employing several steps of constant applied stress. We observe an intense acoustic activity, exhibiting a strong intermittent character (see Fig. 1 inset). We measure the energy associated with each acoustic burst and analyse its statistical properties. In Fig. 1 we show that the probability distribution of energy burst intensities exhibits a power-law behaviour spanning several decades. This fact is an indication that a large number of dislocations move cooperatively in an intermittent fashion. A similar behaviour has been observed in the Portevin–LeChatelier effect[13], a plastic instability where the intermittent flow is ruled by the interaction of dislocations and diffusing solute atoms. The intermittency observed in our case is different as we only have interacting dislocations subject to an external stress, without any other alien element interfering with their dynamics.

Multiscale properties and pattern formation are ubiquitous in plastic materials and we expect that the large dynamical fluctuations observed in ice compression experiments are also a prevalent feature of plastic deformation micromechanics. This general picture implies that the experimental phenomenology should be reproducible in simple numerical simulations of discrete dislocation dynamics that preserve the relevant characteristics of the system under study. As in previous dislocation dynamics models[4–7], we consider a two-dimensional cross-section of the crystal (that is, the xy plane), and randomly place N straight-edge dislocations gliding along a single slip direction parallel to their respective Burgers vectors $\mathbf{b}$ (that is, the x direction). This implies that we have point-like dislocations moving along fixed lines parallel to the x axis. This simplification effectively describes materials like ice crystals that, owing to their strong plastic anisotropy, deform by glide on a single

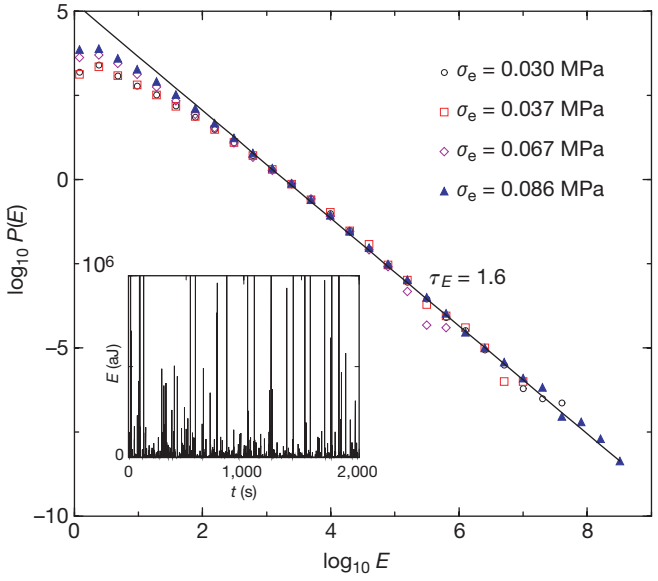

Figure 1 Statistical properties of the acoustic energy bursts recorded in ice single crystals under constant stress. The main figure shows the distribution of energy bursts for the different loading steps. The cut-offs depend slightly on the applied stress, but the power-law exponent remains the same. The fit yields an exponent $\tau_E = 1.60 \pm 0.05$. Inset, a typical recorded acoustic signal. The creep experiment is performed at $T = -10\,°C$ under different constant compression stresses ranging from $\sigma = 0.58$ MPa to $\sigma = 1.64$ MPa. The stress is applied at an angle with respect to the c axis, giving rise to a small resolved shear stress acting across the glide plane ($\sigma_e = 0.030$ MPa–0.086 MPa). The frequency bandwidth of the transducer was 10–100 kHz. The amplitude range between the minimum and the maximum recordable thresholds is 70 dB, that is, a range of seven orders of magnitude in energy.

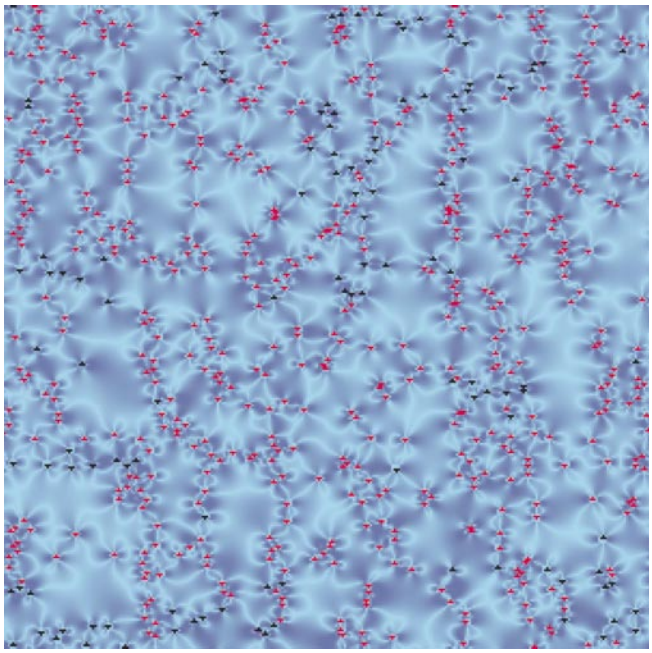

Figure 2 Snapshot of the total stress field and arrangement of dislocations in a numerical simulation with $v_\sigma = 0.025$. We observe metastable structure formation (dipoles and walls) and the associated stress field which goes from light blue (low values) to dark blue (high values). The complex low-stress pathways joining dislocations are the result of the anisotropic elastic interactions. Dislocations moving at low velocities (lower than v_σ) are depicted in red, while those moving at higher velocities are depicted in black. Most dislocations in walls are moving slowly, whereas isolated ones tend to move at higher speed. In the simulations, an initial number of $N_0 = 1{,}500$ dislocations are randomly distributed on a square cell of size $L = 300$. Their Burgers vectors are randomly chosen to be $+b$ or $-b$ with equal probability. In the absence of external stress, we first let the system relax until it reaches a metastable arrangement. The number of remaining dislocations is then $N \approx 700$. At this point, we apply a constant shear stress and study their evolution. To avoid the discontinuities arising from truncating long-range elastic interactions in equation (1), we resort to the Ewald summation method. We have thus exactly taken into account the interaction of a dislocation with all the infinite periodic images of another dislocation in the same cell.

slip system. An edge dislocation with Burgers vector **b** located at the origin gives rise to a shear stress σ_s at a point $\mathbf{r} = (x, y)$ of the form

$$\sigma_s(\mathbf{r}) = b\mu \frac{x(x^2 - y^2)}{2\pi(1-\nu)(x^2+y^2)^2} \quad (1)$$

where μ is the shear modulus and ν is the Poisson ratio[1]. This long-range stress is responsible for mutual interactions among dislocations which are important in all dislocation dynamics models[4–7]. Under a constant external stress σ_e, dislocation i performs an overdamped motion along the x direction described by the following equation

$$\eta \frac{dx_i}{dt} = b_i \left(\sum_{m \neq i} \sigma_s(\mathbf{r}_m - \mathbf{r}_i) - \sigma_e \right) \quad (2)$$

where η is the effective friction and b_i is the Burgers vector. Throughout the simulations, we will be dealing with dimensionless quantities after setting the distance scale $b = 1$, and the timescale $t_o \equiv \eta b/(\mu/2\pi(1-\nu)) = 1$.

Other essential ingredients commonly introduced in most dislocation dynamics models[4–7] are the mechanisms for dislocation (1) annihilation and (2) multiplication. (1) When the distance between two dislocations is of the order of a few Burgers vectors, the high stress and strain conditions close to the dislocation core invalidate the results obtained from a linear elasticity theory (equation (1)). In these instances, phenomenological nonlinear reactions describe more accurately the real behaviour of dislocations in a crystal. In our model, we annihilate two dislocations with opposite Burgers vectors when the distance between them is shorter than $2b$. (2) The activation of Frank–Read sources[1] is accepted as the most relevant dislocation multiplication mechanism under creep deformation. The activation of Frank–Read sources has been observed in ice crystals, along with more specific multiplication processes[19]. Because an accurate multiplication mechanism cannot be simulated in a two-dimensional point-dislocation model, we have implemented various phenomenological procedures. A simple way of taking into account the new dislocation loops generated at different sources within the crystal is the random introduction of opposite-sign dislocation pairs in the cross-section under consideration. The rate and frequency of this creation process depend solely on the external stress σ_e. We have checked that other multiplication rules in which the creation rate depends on the local stress yield similar results.

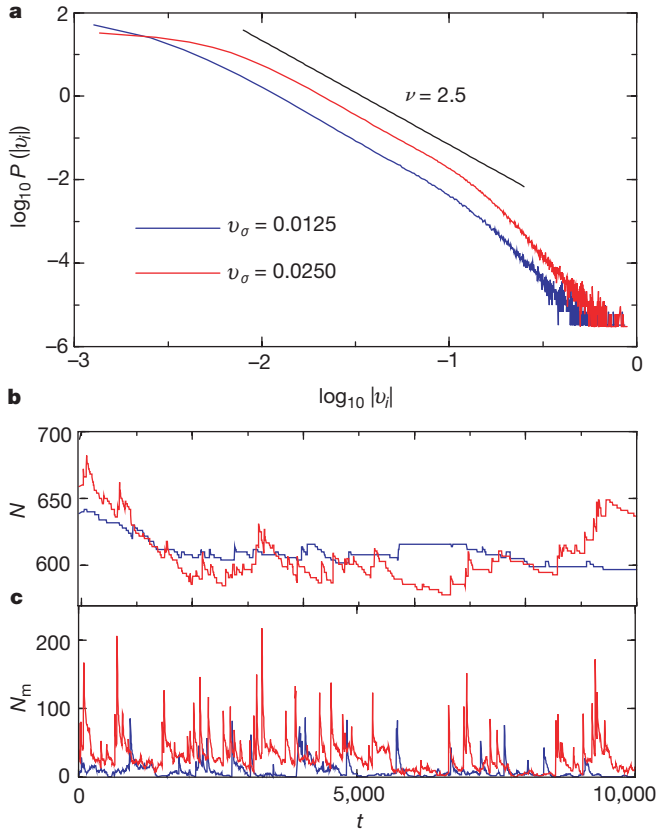

Figure 3 Statistical properties of dislocation velocities and density obtained in numerical simulations. **a**, Probability density of the individual dislocation velocities $|v_i|$ in the stationary state. The black line is a least-squares fit of the intermediate data points. We obtain an exponent $\nu = 2.5$ for the scaling of the intermediate velocities. **b**, Time evolution of the total number of dislocations in the cell. **c**, Fraction of fast-moving dislocations for a given run of the simulations.

In the initial stage of the simulations, the system relaxes slowly and the average strain-rate decreases until it reaches a constant value which depends on the applied stress, that is the stationary creep regime. By monitoring the activity in a single run, we observe that most dislocations are arranged into metastable structures (such as walls and cells) moving at a very slow rate (see Fig. 2 and Supplementary Information). A smaller fraction of dislocations, however, move intermittently at much higher velocities, giving rise to sudden increases of the plastic strain. In Fig. 3a, we plot the probability density of finding an individual dislocation moving with a velocity $|v_i|$. Already at the level of individual dislocations, the velocity distribution $P(|v_i|)$ is quite broad and exhibits power-law behaviour for velocity values larger than the external stress-induced velocity $v_\sigma = b\sigma_e/\eta$ (we have considered two values of v_σ: 0.0125 and 0.025).

In the presence of a large number of dislocations, the acoustic signal that is detected experimentally is due to the superposition of the waves emitted by each moving dislocation[15]. In particular, it has been shown that a single dislocation performing a sudden movement with velocity v_0 for a short time τ gives rise to an acoustic wave whose amplitude is proportional to v_0 (ref. 15). The high-amplitude pulses detected in the experiment cannot be ascribed to uncorrelated emissions from each individual dislocation, but rather to the cooperative motion of several dislocations occurring, for example, after the activation of a Frank–Read source, or if a dislocation cluster breaks apart. To gain further insight into this behaviour, in Fig. 3b and c, we show the evolution of the total number of dislocations as well as that of the fast-moving dislocations, that is, dislocations moving faster than if they were moving only under the action of the external stress, $v_i > v_\sigma$ (other threshold values yield equivalent results). After the injection of a few new dislocations or the annihilation of a dislocation pair, several other dislocations start to move and rearrange, not necessarily in the close vicinity of the triggering event. To quantify this effect, we measure the collective velocity $V = \Sigma'|v_i|$ of the fast-moving dislocations and define the acoustic energy as $E = V^2$ (ref. 17). In the inset of Fig. 4, we see that the signal $E(t)$ consists of a succession of intermittent and pronounced bursts, each one signalling the onset of collective dislocation rearrangements. The slow and continuum motion of dislocation structures ($v_i < v_\sigma$) is not considered as it only sets up a background noise signal which cannot be detected experimentally. In Fig. 4 we show that the distribution of energy bursts, obtained by sampling the signal over different times and realizations, decays very slowly, spanning various decades. For intermediate values, the distribution shows an algebraic decay with an exponent $\tau_E = 1.8 \pm 0.2$, in reasonable agreement with experiments (see Fig. 1). The maximum number of dislocations we can handle in our simulations severely restricts the maximum value of the signal in the system. Consequently, the extension of the power-law regime grows with the number of dislocations, but is eventually bounded by the different nature of the extremes statistics.

The broadly distributed intermittency resulting from the statistical analysis can be interpreted as a nonequilibrium transport

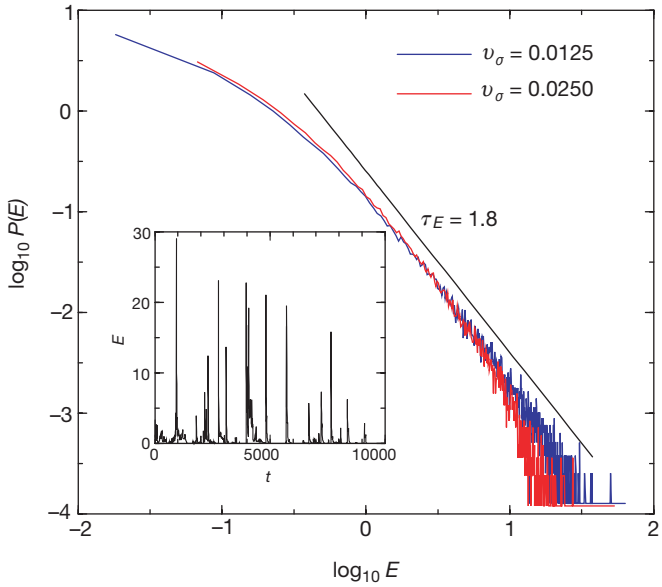

Figure 4 Statistical properties of the energy bursts obtained in numerical simulations. In the model, we define the acoustic energy $E = V^2$ from the collective velocity $V = \Sigma_i' |v_i|$ of the fast-moving dislocations. The time evolution of E for a given simulation run is plotted in the inset. The energy distribution averaged over time and over 100 realizations with different initial conditions is plotted in the main graph. The black line represents the best fit of the intermediate data points. We obtain an exponent $\tau_E = 1.8 \pm 0.2$ for both values of the external stress.

phenomenon with scaling properties. Scaling behaviour is usually associated with the proximity of a critical point and is characterized by a high degree of universality. Critical exponents only depend on a few fundamental parameters such as the effective dimensionality and the basic symmetries of the system. Specifically, the reasonable quantitative agreement between our model and the experimental data is due to the strong plastic anisotropy present in ice single crystals, which can thus be well described by a two-dimensional model. Although the quantitative results we obtain should be restricted to the case of single slip systems, the general features of the observed intermittent flow regime appear to be generic in plastic deformation[11,12]. The particular universality class will depend on the effective dimensionality of each specific material as well as the particular deformation mechanism, and one can still expect to obtain the right critical exponents from simplified models if the relevant symmetries are correctly taken into account.

The close-to-criticality nonequilibrium framework suggests possible analogies with elastic manifolds driven in random media such as fluid flow in porous media, vortices in superconductors, and charge density waves[20]. In all of these systems, a critical value of the driving force separates a static regime from a moving one, and scaling is observed only close to this point. The intermittent behaviour close to criticality is in these cases associated with static random heterogeneities which exert space-dependent pinning forces on the moving objects. On the contrary, the present dislocation dynamics model, as well as the ice experiment, does not contain any quenched source of pinning forces. Dislocations themselves, through the various structures such as dipoles and walls, generate a pinning force landscape in which the dynamics is virtually frozen, that is, a slow dynamics state. Creation and annihilation mechanisms, often triggered by the presence of unsettled dislocations, allow the system to jump between slow dynamics states through bursts of activity. This behaviour is reminiscent of driven-dissipative self-organizing systems that achieve criticality in the limit of very slow driving[21].

This emerging picture poses many basic theoretical questions. Is there a critical stress value below which the system decays into a slow dynamics state? Can the large dynamical fluctuations be associated with a diverging response function and thus be related to a critical point? Can we derive scaling laws relating the various observed exponents, as suggested by the theory of critical phenomena? The answers to all these questions pave the way to the nonequilibrium statistical theory of dislocation motion that is needed for a deeper understanding of the micromechanics of plastic deformation. □

Received 26 October 2000; accepted 26 January 2001.

1. Hirth, J. P. & Lothe, J. *Theory of Dislocations* (Krieger, Malabar, Florida, 1992).
2. Hähner, P., Bay, K. & Zaiser, M. Fractal dislocation patterning during plastic deformation. *Phys. Rev. Lett.* **81,** 2470–2473 (1998).
3. Zaiser, M., Bay, K. & Hähner, P. Fractal analysis of deformation-induced dislocation patterns. *Acta Mater.* **47,** 2463–2476 (1999).
4. Lepinoux, J. & Kubin, L. P. The dynamic organization of dislocation structures: A simulation. *Scr. Metall.* **21,** 833–838 (1987).
5. Amodeo, R. J. & Ghoniem, N. M. Dislocation dynamics. I. A proposed methodology for deformation micromechanics. *Phys. Rev. B* **41,** 6958–6967 (1990).
6. Groma, I. & Pawley, G. S. Computer simulation of plastic behaviour of single crystals. *Phil. Mag. A* **67,** 1459–1470 (1993).
7. Fournet, R. & Salazar, J. M. Formation of dislocation patterns: Computer simulations. *Phys. Rev. B* **53,** 6283–6290 (1996).
8. Gil Sevillano, J., Bouchaud, E. & Kubin, L. P. The fractal nature of gliding dislocation lines. *Scr. Metall. Mater.* **25,** 355–360 (1991).
9. Thomson, R. & Levine, L. Theory of strain percolation in metals. *Phys. Rev. Lett.* **81,** 3884–3887 (1998).
10. Neuhäuser, H. in *Dislocations in Solids* (ed. Nabarro, F. R. N.) 319–440 (North-Holland, Amsterdam, 1983).
11. Becker, R. & Orowan, E. Über sprunghafte Dehnung von Zinkkristallen. *Z. Phys.* **79,** 566–572 (1932).
12. Bengus, V. Z., Komnik, S. N. & Shititelman, O. B. Dislocation multiplication as a controlling factor of work-hardening. *Phys. Stat. Sol.* **14,** 215–222 (1966).
13. Ananthakrishina, G. *et al.* Crossover from chaotic to self-organized critical dynamics in jerky flow of single crystals. *Phys. Rev. E* **60,** 5455–5462 (1999).
14. Hähner, P. On the foundations of stochastic dislocation dynamics. *Appl. Phys. A* **62,** 473–481 (1996).
15. Rouby, D., Fleischman, P. & Duvergier5, C. Un modèle de source d'émission acoustique pour l'analyse de l'émission continue et de l'émission par salves: I. Analyse théorique. *Phil. Mag. A* **47,** 671–687 (1983).
16. Weiss, J. & Grasso, J. R. Acoustic emission in single crystals of ice. *J. Phys. Chem. B* **101,** 6113–6117 (1997).
17. Weiss, J., Lahaie, F. & Grasso, J. R. Statistical analysis of dislocation dynamics during viscoplastic deformation from acoustic emission. *J. Geophys. Res.* **105,** 433–442 (2000).
18. Duval, P., Ashby, M. F. & Andermann, I. Rate-controlling processes in the creep of polycrystalline ice. *J. Phys. Chem.* **87,** 4066–4074 (1983).
19. Petrenko, V. F. & Whitworth, R. W. Structure of ordinary ice I_h. Part II: Defects in ice. Vol. 2: Dislocations and plane defects. (US Army Cold Regions Research and Engineering Laboratory Special Report 94-12, Hanover, New Hampshire, 1994).

20. Kardar, M. Nonequilibrium dynamics of interfaces and lines. *Phys. Rep.* **301,** 85–112 (1998).
21. Jensen, H. J. *Self-Organized Criticality* (Cambridge Univ. Press, Cambridge, 1998).

Supplementary information is available on *Nature*'s World-Wide Web site (http://www.nature.com) or as paper copy from the London editorial office of *Nature*.

Acknowledgements

We thank R. Pastor-Satorras, M. Rubí, A. Scala and M. Zaiser for useful discussions, and O. Brisaud, and F. Dominé for help in the preparation of single crystals. We acknowledge partial support from the European Network contract on "Fractal Structures and Self-organization". J.W. is supported by the "Action thématique innovante" of Institut National des Sciences de l'Univers-CNRS. Acoustic emission monitoring devices were financed by Université Joseph Fourier.

Correspondence and requests for materials should be addressed to M.-C.M. (e-mail: carmen@ffn.ub.es).

Varied pore organization in mesostructured semiconductors based on the $[SnSe_4]^{4-}$ anion

Pantelis N. Trikalitis*, K. Kasthuri Rangan*, Thomas Bakas† & Mercouri G. Kanatzidis*

** Department of Chemistry, Michigan State University, East Lansing, Michigan 48824, USA*
† Department of Physics, University of Ionnina, Ioannina, 45110, Greece

Open framework metal chalcogenide solids, with pore sizes in the nano- and mesoscale, are of potentially broad technological and fundamental interest in research areas ranging from optoelectronics to the physics of quantum confinement[1,2]. Although there have been significant advances in the design and synthesis of mesostructured silicas[3,4], the construction of their non-oxidic analogues still remains a challenge. Here we describe a synthetic strategy that allows the preparation of a large class of mesoporous materials based on supramolecular assembly of tetrahedral Zintl anions $[SnSe_4]^{4-}$ with transition metals in the presence of cetylpyridinium (CP) surfactant molecules. These mesostructured semiconducting selenide materials are of the general formulae $(CP)_{4-2x}M_xSnSe_4$ (where $1.0 < x < 1.3$; M = Mn, Fe, Co, Zn, Cd, Hg). The resulting materials are open framework chalcogenides and form mesophases with uniform pore size (with spacings between 35 and 40 Å). The pore arrangement depends on the synthetic conditions and metal used, and include disordered wormhole, hexagonal and even cubic phases. All compounds are medium bandgap semiconductors (varying between 1.4 and 2.5 eV). We expect that such semiconducting porous networks could be used for optoelectronic, photosynthetic and photocatalytic applications.

The discovery of a general synthetic pathway to ordered mesoporous silicates by the Mobil group[3,4] led to new hybrid mesoporous solids and has captured the imagination of many materials scientists. During the past decade, assembling inorganic molecular species in the presence of long-chain organic liquid-crystal templates has been used extensively to construct mesoporous oxides. In general, the synthetic approaches involve the organized polymerization of the basic tetrahedral $[SiO_4]^{4-}$ anion in the presence of various surfactants[5–7]. Non-oxide porous solids, however, are also important[8,9], because they may impart electronic properties to the framework, and thus make mesoporous solids into nano-electronic materials[7,10]. Nevertheless, rational synthetic routes to such systems remain a challenge. A promising pathway for the construction of non-oxide mesoporous solids such as sulphides, selenides or tellurides is the supramolecular assembly of suitable chalcogenide anion species in the presence of metals. Recently, the synthesis of mesostructured solids based on the adamantane $[Ge_4Q_{10}]^{4-}$ (where Q = S, Se) clusters and metal ions (such as Zn^{2+}, Co^{2+}, Ni^{2+}, Cu_2^{2+}) has been described. Depending on preparation conditions, these materials possess either a disordered three-dimensional framework structure or a regular hexagonal symmetry[11–14]. The energy bandgaps of these solids however are still too high for electronic applications.

We describe the design and synthesis of mesostructured materials based on the elementary tetrahedral Zintl anion $[SnSe_4]^{4-}$. This anion is a chemical and structural analogue of the SiO_4 unit and we expect it to yield topologically similar structures. It is also smaller and heavier than the $[Ge_4S_{10}]$ cluster and more likely to yield narrow-gap semiconductors. Spatially controlled assembly of $[SnSe_4]^{4-}$ anions[15] in formamide with various divalent metals in the presence of cetylpyridinium molecules as the surfactant template resulted in the formation of new mesophases. These materials, indicated as $(CP)_{4-2x}M_xSnSe_4$ (where $1.0 < x < 1.3$; M = Mn^{2+}, Fe^{2+}, Co^{2+}, Zn^{2+}, Cd^{2+} and Hg^{2+}), show uniform pore size and large diversity in pore organization, depending on the metal, and ranging from wormhole to hexagonal to cubic. The elemental composition $(CP)_{4-2x}M_xSnSe_4$ was determined by energy-dispersive microprobe analysis (EDS), elemental C, H, N and thermogravimetric analysis (TGA). In all samples the ratio of Sn:Se was very close to 1:4, in agreement with the expected ratio for the tetrahedral $[SnSe_4]^{4-}$ anions. Infrared spectroscopy confirmed the presence of cetylpyridinium ions in the mesostructured $(CP)_{4-2x}M_xSnSe_4$ solids. A summary of the analytical and other data is shown in Table 1.

X-ray diffraction (XRD) patterns of the products show a strong, sharp peak at low scattering angles corresponding to (100) reflections (Fig. 1). The d_{100} values, which represent the pore–pore separation, vary with the transition metal used, ranging between 35 Å and 40 Å (see Table 2). The XRD patterns also show a broad higher-order peak ($2\theta \approx 4$–5 degrees), corresponding to overlapping higher-order reflections (110) and (200) which can be indexed to a hexagonal lattice as observed by transmission electron

Table 1 Elemental analysis, colours and bandgaps for mesostructured metal tin selenides

Sample	Sn:Se$_4$*	M:Se$_4$*	Percentage of C, H, N	M:Se$_4$†	Colour	Bandgap (eV)
Mn	1.01	0.90	44.71, 7.10, 2.25	1.03	Orange	2.0
Fe	0.91	1.22	38.40, 6.23, 2.05	1.28	Dark brown	1.4
Co	0.98	0.94	48.35, 6.64, 2.36	1.19	Dark brown	
Zn (cubic)	0.99	0.86	40.28, 6.17, 2.18	1.20	Yellow-orange	2.5
Zn (hex)	0.96	0.85	41.58, 6.44, 2.29	1.15	Yellow	2.5
Cd	0.92	1.23	36.90, 6.01, 2.28	1.23	Yellow	2.4
Hg	1.03	1.09	34.65, 5.52, 1.92	1.20	Dark orange	2.2

* Based on energy-dispersive spectroscopy (EDS) results. Semiquantitative microprobe analyses (EDS) were performed on a JEOL JSM-6400 scanning electron microscope (SEM) equipped with a Noran EDS system. Data acquisition was performed several times in different areas of the samples using an accelerating voltage of 25 kV and 60-s accumulation time. Quoted values were obtained from an average of four measurements.
† Calculated values according to the formula $(CP)_{4-2x}M_xSnSe_4$, based on C, H, N results. C, H, N analyses were performed with Perkin Elmer Series II CHNS/O Analyzer 2400.